LA-UR- 10-00113

Approved for public release;
distribution is unlimited.

Title:	Three dimensional simulations of Richtmyer-Meshkov instabilities in shock-tube experiments.
Author(s):	Gowardhan, A.A., Grinstein, F.F., and Wachtor, A.J.
Intended for:	To be presented at the AIAA Aerospace Sciences Meeting, Orlando, FL, January 4-7, 2010.

Form 836 (7/06)

THREE DIMENSIONAL SIMULATIONS OF RICHTMYER-MESHKOV INSTABILITIES IN SHOCK-TUBE EXPERIMENTS

A.A. Gowardhan, F.F. Grinstein, and Adam Wachtor

Applied Physics Division, X-3-MA
MS F644, Los Alamos National Laboratory
Los Alamos, NM 87545

Abstract

In the large eddy simulation (LES) approach large-scale energy-containing structures are resolved, smaller (presumably) more isotropic structures are filtered out, and unresolved subgrid effects are modeled. Extensive recent work has demonstrated that predictive simulations of turbulent velocity fields are possible based on subgrid scale modeling implicitly provided by a class of high-resolution finite-volume algorithms. This strategy is called implicit LES. The extension of the approach to the substantially more difficult problem of material mixing is addressed, and progress in representative shock-driven turbulent mixing studies is reported.

BACKGROUND

It is not feasible to compute high Reynolds-number (Re) turbulent flows by directly resolving all scales of motion and material interfaces; instead, macroscale portions of the unsteady turbulent motion are computed while the rest of the flow physics including molecular diffusion and other micro scale physics (e.g., combustion) remains unresolved. In large eddy simulation (LES) [1], the large energy containing structures are resolved whereas the smaller structures are filtered out and their unresolved subgrid scale (SGS) effects are modeled. In the absence of an established universal theory of turbulence, the construction of SGS models is pragmatic and based primarily on empirical information.

Adding to the physics based difficulties in developing and validating SGS models, truncation terms due to discretization are comparable to SGS models in typical LES strategies [2], and LES resolution requirements are mostly prohibitively expensive for practical flows and regimes. Implicit LES [3] (ILES) effectively addresses the seemingly insurmountable issues posed to LES by under-resolution, by relying on the use of SGS modeling and filtering provided implicitly by a class of physics capturing numerics. Popular high-resolution finite-volume methods such as flux-corrected transport, the piecewise parabolic method, total variation diminishing, Godunov, and hybrid algorithms are being used for ILES; extensive verification and validation in areas of engineering, geophysics, and astrophysics has been reported [3]. *The extension of ILES to the substantially more difficult problem of under-resolved material mixing driven by under-resolved velocity field and initial conditions (ICs) is the subject of the present paper.*

In many applications of interest, turbulence is generated by shock waves via Richtmyer-Meshkov instabilities (RMI) (e.g., [4]). The instability results in vorticity being introduced at material interfaces by the impulsive loading of the shock wave. RMI add the complexity of shock waves and other compressible effects to the basic physics associated with mixing;

compressibility further affects the basic nature of material mixing when mass density and material mixing fluctuation effects are not negligible. Because RMI are shock-driven, resolution requirements make DNS impossible even on the largest supercomputers; the state-of-the-art simulations (e.g., [5]) use hybrid methods which switch between shock-capturing schemes and conventional LES depending on the local flow conditions.

Given that ILES is based on locally-adaptive, non-oscillatory, finite-volume methods it is naturally suited to emulate shock physics. The unique combination of shock and turbulence emulation capabilities supports direct use of ILES as an effective simulation *anzatz* for RMI. Here, we test a particular ILES strategy in the case of shock-tube experiments for which previously reported data [4,5,7] can be used for validation purposes. The present simulations model the Caltech planar [4,5] and the Los Alamos National Laboratory (LANL) P-23 gas-curtain shocktube experiments [7]. The ILES tested here is based on a nominally-inviscid simulation model which solves the conservation equations for mass density, momenta, total energy, and partial material densities convected as separate scalars. The LANL RAGE code [6] solves the multi-material compressible conservation equations for mass density, momenta, total energy, and partial mass densities, using a 2nd-order Godunov scheme, adaptive mesh refinement (AMR), a variety of numerical options for gradient terms – limiters, and optional interface treatments (not used here). The van Leer limiter was chosen in the present simulations. Two-dimensional (2D) RAGE studies of RMI have been previously reported [8,9].

PLANAR SHOCK-TUBE EXPERIMENTS

We focus on the planar shock-tube experiments in [4], involving high (SF6) and low density (air) gases, presumed geometries of the membranes and the wire mesh initially separating the gases, and reshock off an end-wall (Figure 1). The mixing-layer growth is affected by the initial interaction of shock and material-interface – with direct distinct imprint of the mesh spacing on the initial contact discontinuity shape, and significant further effects occurring after reshock. The contact discontinuity between air and SF6 is modeled as a jump in density using ideal gases with γ=1.4 and γ=1.076, respectively, with constant pressure across the initial interface at rest. A shocked air region is created upstream satisfying the Rankine-Hugoniot relations for a Mach 1.5 shock. The shock propagates in the (x) direction through the contact discontinuity and reflects at the end of the simulation box on the right. Periodic BCs conditions are imposed in the transverse (y,z) directions.

A crucial issue when simulating turbulent flow instabilities such as considered here is that of modeling the insufficiently-characterized initial contact-discontinuity deformations in the laboratory experiments. The inherent difficulties with the open problem of predictability of material stirring and mixing by under-resolved numerically generated multi-scale turbulent velocity fields, are now compounded with the inherent sensitivity of turbulent flows to ICs [10].

The surface displacement of the material interface in the RMI experiments has been modeled combining well-defined modes with random perturbation components. Examples of IC modeling strategies used in the reported work included using: 1) *S+L* deformation [11] combining a short (*S*) *egg-crate* mode – chosen to represent the result of pushing the membrane through the wire mesh, and superimposed distortion of the wire mesh on a longer (L) scale of the order of a characteristic shocktube transverse dimension; 2) $S+L+\phi$ [12], or, 3) $S+\phi$ [5], where ϕ is a spatially random distribution intended to break the presumed characteristic interface symmetries. The $S+\phi$ strategy is used here to model the initial interface conditions. We define the perturbation in terms of a prescribed range of modes $\lambda\min < \lambda < \lambda\max$ [13], i.e.,

$$dx(y,z) = S + \phi$$
$$= A_1 \left|\sin(k_o y)\sin(k_o z)\right| + A_2 \sum_{n,m} a_{n,m} \sin(k_n y + \varphi_n)\sin(k_m y + \chi_m)$$

where $dx(y,z)$ is the local interface deformation, $\lambda_o = \pi/k_o = L/12$ is the characteristic length scale of the *egg crate* mode, A_1=0.25 cm, A_2=0.025 cm is the prescribed standard deviation of the perturbation, $k_n = 2\pi n/L$, $k_m = 2\pi m/L$, random coefficients $-1/2 < a_{m,n} < +1/2$, random phases φ_n, χ_m, and the participating modes are constrained by the requirement,

$$\lambda_{\min} < L/\left[2\pi\sqrt{(n^2+m^2)}\right] < \lambda_{\max}.$$

Simulations were performed for a variety of grid resolutions and types of perturbations superimposed to the mode *S*. The selected representative cases discussed here (Table 1, Figs. 2) involve: (a), $(\lambda_{\min}, \lambda_{\max}) = (0.4\lambda_o, 4\lambda_o)$ – *short* perturbation, (b), $(\lambda_{\min}, \lambda_{\max}) = (4\lambda_o, 12\lambda_o)$ – *long* perturbation, and, (c) *no* perturbation (A_2=0).

Table 1. Planar Shock-tube Simulations

Case	$\Delta_{\min}$(cm)	AMR	NX_{max}	NY_{max}	NZ_{max}	Max Grid points	ϕ	perturbation
RUN1 (2D)	0.1	YES	820	240	-	196,800	A_2=0.025 cm	short
RUN2 (2D)	0.05	YES	1640	480	-	787,200	A_2=0.025 cm	short
RUN3 (3D)	0.1	YES	820	240	240	28,55,528	A_2=0.025 cm	short
RUN4 (3D)	0.05	YES	1640	480	480	177,856,000	A_2=0.025 cm	short
RUN5 (3D)	0.1	YES	820	240	240	28,55,528	A_2=0.025 cm	long
RUN6 (3D)	0.1	YES	820	240	240	28,55,528	A_2=0.000 cm	no

Analysis of the simulation data is based on using ensemble (cross-stream) averaged quantities, e.g., for the planar case

$$\langle f \rangle(x) = \frac{1}{A}\int f(x,y,z)dydz \ , \ A = \int dydz$$

Integral flow quantities used in the analysis below are defined as follows

$$\rho = \langle \rho \rangle + \rho',$$
$$\tilde{u}_i = \langle \rho u_i \rangle / \langle \rho \rangle,$$
$$u_i = \tilde{u}_i + u_i' \ ,$$
$$\mathrm{R}_{ij} = \left\langle \rho u_i' u_j' \right\rangle,$$
$$2\langle K \rangle = \mathrm{R}_{mm} \ ,$$
$$\psi = \left\langle \frac{\rho_{SF_6}}{\rho} \right\rangle,$$
$$TKE = \int K dx dy dz$$
$$\Omega = \int \rho \omega^2 \, dx \, dy \, dz \ ,$$

where the tilde denotes mass-weighted (*Favre*) averaging, summation over repeated indices is assumed, R is the Reynolds stress, K denotes turbulent kinetic energy, ρ and ρ_{SF6} are the mass density and SF_6 mass-density, respectively, the u_i are the velocities, w is the vorticity magnitude, and W is the mass-weighted enstrophy. A material mixing-layer thickness θ is defined as in [5] by, $\theta = 4\int \psi(x)[1-\psi(x)]dx$, where $\psi(x) = \left\langle \frac{\rho_{SF_6}}{\rho} \right\rangle$.

The diagram in Fig.3 shows the evolution and interaction of the M=1.5 shock and air/SF_6 interface for a selected representative case, in good agreement with similar ones in the other cases considered here as well as in previous work [4,5]. The air/SF_6 interface is shocked at t = 0 ms, reshocked by the primary reflected shock at t~3.5 ms, and then by the reflected rarefaction at t ~ 5ms. The mixing layer is reshocked further by weaker secondary reflected shocks at later times.

Figures 4 show characteristic flow visualizations in terms of isosurfaces of the SF_6 mass-fraction at selected times. Figures 5 show spectra of the turbulent kinetic energy K as a function of time. Figures 6 show corresponding probability distribution functions (PDFs) of relevant velocity functions. Effects of grid resolution on the spectral and PDF results are addressed on Figs. 7 (and in Fig. 8a). Our spectral and PDF analysis are based on velocity data in a slab chosen around the center of the mixing layer at each time, and constrained in the x-direction by requiring that the SF_6 mass-fraction be greater than 0.25. Reported spectra are the result of averaging 1D (y- and z-direction) spectra for each cross-stream plane within the slab, and then over all planes in the slab. In all cases, the peak spectral amplitude at $kL/2\pi=1$ at t=0 corresponds to the dominant *egg crate* mode (wavelength $\lambda_o/2$) and the lower-amplitude regularly spaced peaks associated to its harmonics. Before reshock, the *random interface perturbation* distorts the S mode and leads to less mixing-layer growth compared to the *non-perturbed* case. Figures 5 show that the turbulent kinetic energy decreases after shocked time (t=0), and then increases at reshock – as energy is again deposited through baroclinic production of vorticity at the material interfaces; shorter wavelengths get populated as time evolves, and self-similarity of the spectra becomes increasingly apparent.

The spectral peak associated with the S mode in the spectra disappears after reshock for the perturbed cases. K increases again as the mixing layer gets reshocked further by the reflected-rarefaction (t > ~5 ms),; by this time, the fundamental *egg crate* mode has completely disappeared in the *randomly perturbed* case. For t >6 ms, the spectra decays self-similarly and exhibits a power-law behavior consistent with Kolmogorov's $k^{-5/3}$ law, whereas the *fundamental* mode is still dominant in the *non-perturbed* case. The late-time trends toward self-similar behavior are also clearly suggested in terms of the PDF's of the vorticity magnitude, strain-rate magnitude, and velocity derivatives in Figs. 6. Increasing the resolution effectively results on a longer inertial range on the spectra for the late-times (Figure 7a), when isotropic flow characteristics are also suggested by the good agreement with corresponding PDF's of DNS data of incompressible isotropic turbulence [14] (Fig. 7bc); *these results can be consistently characterized by a higher effective Reynolds number associated with the higher resolution* [15].

Predicted mixing measures are compared with experiments [4] and previous LES [5] in Figs. 8. IC effects on the integrated turbulent kinetic energy *TKE* and mass-weighted enstrophy W are shown on Figures 9-10. Figure 8a demonstrates effects of resolution on the *short perturbation* results, while Fig. 8b examines effects of various IC perturbations (at a fixed resolution 0.1cm). Figure 8a shows the variation of θ as a function of time for the various cases with *randomly perturbed interface* (Table 1). There is significantly slower 2D growth after reshock (t~3.5 ms) due to the absence of vortex stretching; the sensitivity of the predicted mixing-layer thickness to grid resolution reflects on differences on: 1) initial interface conditions resolution, and 2) RMI growth rates (a function of *effective ILES Re*). The results indicate early-time consistency of predicted growth rates with those previously reported [4,5], and show distinct IC effects for the late times (for t > 5ms) – e.g., reduced mixing width predicted after reshock by RUN 4

(compared to RUN 3). The three-dimensional (3D) cases perform similarly in the shocked region, but after reshock, predicted growth rate with RUN 4 (finest grid) compares better with the experiments [4] and previous simulations [5]. Late-time discrepancies reflect on cumulative effects due to impact of interface IC details (i.e., similar but different spectral content of ϕ), as well as actual implementation of numerical schemes and wall boundary conditions.

Figure 8b shows the variation of the mixing layer thickness θ as a function of time for the different ICs considered. Overall, the predicted mixing widths for all cases are very similar before reshock (< 3.5 ms), when mixing width for the short *perturbation* case is slightly greater; a thicker mixing layer is associated with breaking of the *S* mode due to the perturbations. After reshock, the opposite phenomenon is observed; predicted mixing width is the least for the *short perturbation* case – reflecting on the presence of fewer large scale coherent vortical structures, and consistently smaller *TKE* and Ω (Figs. 9 and 10). Figure 9 shows the variation of TKE as a function of time for two different types of averaging: volumetric and Favre (mass-weighted) averaging, indicating consistently higher Favre averaged TKE values.

SHOCKED GAS-CURTAIN EXPERIMENTS

An SF_6 gas curtain is formed by forcing SF_6 through a linear arrangement of round nozzles into the shocktube test section [7]. Once a steady state is achieved, the gas curtain is shocked (Mach numbers, M=1.2), and its later evolution subject to Richtmyer-Meshkov flow instabilities, transition, and nonequilibrium turbulence phenomena is investigated based on high resolution data acquisition for shocked and reshocked cases (Figure 11) at a selected horizontal plane at approximately 2cm below the beginning of the gas curtain. Previous 2D RAGE simulations of the experimental shocked gas-curtain observations have been reported [9].

Only relative SF_6 intensities, C/C_{max} in the said horizontal slice are acquired, where C_{max} is the peak concentration at that slice. To address the possible impact of not knowing the actual value of C_{max}, several 2D RAGE simulations of the shocked SF_6 gas-curtain were carried out assuming various values of C_{max} in the range of 40% to 80% of its nominal value at the nozzle exits. Typical simulation results on 2D evolution of RMI are illustrated in Fig. 12. The growth of the RMI triggered vortical structures is found be very dependent (Fig. 13) on C_{max}, so that it is very important to accurately approximate the value of C_{max} in the experiments.

Simulation of the 3D Gas-Curtain

The possible important role of 3D instabilities is suggested by the recently reported simulations of a shocked SF6 column [16]. The laboratory experiments have not yet characterized the 3D nature of the SF_6 gas-curtain concentration distributions. C_{max} changes in z direction give rise to

considerable potential 3D effects, and thus, detailed 3D distribution of the initial concentration of SF_6 is also needed. Due to diffusion of SF_6 in air and buoyancy effects, SF_6 concentration gradients develop in the vertical (z) direction and horizontal (x, y) direction. Moreover, additional spreading control applied through suction at the bottom of the laboratory gas curtain is also presently not characterized.

A separate simulation was performed to emulate the physics of SF_6 falling through the test section of the shock tube until a steady state is reached using a 3D Navier-Stokes code which solves incompressible flow in the Boussinesq approximation. The code was previously developed and validated for relevant 2D and 3D test cases [17]. Figure 14 shows the schematic of the computational domain. SF_6 exits through nozzles (R = 0.15 cm) with a presumed inlet velocity V_{in} from the top of the domain. The bottom of the domain can be maintained at a small negative pressure (simulating the suction enforced in the laboratory experiments) such that SF_6 and co-flowing air are removed from the domain and a stable gas-curtain SF6 is maintained. The 3D solution is allowed to evolve in time (Figure 15) until a steady state is reached. The steady state results from the simulations are compared with the available experimental data at a horizontal plane 2 cm from the nozzle exit. The inlet velocity V_{in} was varied from 5 cm/s – 20 cm/s, and suction at the bottom of the gas curtain was not enforced. An optimal match of simulation results and experiments was obtained for V_{in} = 10 cm/s (Figures 16 and 17). Results from this simulation were used as ICs for the RAGE simulation.

Shocked Gas-Curtain RAGE Simulations

The computational domain used in the simulations scales down to ~1/4th of the laboratory test section. Figure 18 shows the SF6 gas curtain IC and a typical computational domain (factors of 2 shorter in the vertical (z) and spanwise (y) directions, while realizing the full scale in the shock (x) direction. Representative simulations with 16-level AMR refinement use ~15 million control volumes; a typical ~1200 μs (real time) simulation requires running for approximately 36 hrs on 512 CPU's on LANL's Lobo supercomputer.

An M=1.20 shock propagates from left to right and impinges the gas curtain at time t = 0 μs (Fig. 19a). As the shock passes through the SF_6 curtain, baroclinic torque is deposited at the air-SF_6 interfaces. Figure 19(b) exemplifies features of the later-time shocked gas-curtain in terms of SF_6 distributions at time t = 600 μs, showing significant 3D effects. Since the concentration of SF_6 is higher near the nozzle exits, bigger structures there reflect on larger vorticity production.

The 3D flow dynamics of the problem is investigated in detail in what follows as a function of ICs, with and without reshock, and grid resolution issues are addressed in this context. The various simulated cases are summarized on Table 2 below. The reshocked and non-reshocked evolutions are visualized in Fig. 20 in terms of SF6 mass-fraction distributions at the z=2cm

plane. Mixedness widths can be calculated based on laboratory and simulation data in terms of a function $\chi(x) = 4\zeta(x)(1-\zeta(x))$ defined on the 2D (z=2cm) slice,

$$\zeta(x) = \int_0^{L_y} \left(\frac{\rho_{SF6}(x, y, z = 2)}{\rho(x, y, z = 2)} \right) dy .$$

The mixedness width is defined as the streamwise distance over which $\chi(x) > 0.95$. Figures 21 compare the mixedness results separately, for the non-reshocked and reshocked case at the baseline resolution (Δx_{min}=0.0125cm). Figure 22 shows the effects of grid resolution on the reshocked case. The figures show good agreement with the laboratory results. The mismatch around reshock time depicted in Fig. 22 (slightly earlier dip in the simulation results) is attributed to somewhat reduced laboratory shock velocity before reshock, and was also noted in the context of the previous 2D simulations [9].

Table 2. Shocked Gas curtain Simulations

Case	Δ_{min}(cm)	AMR	NX_{max}	NY_{max}	NZ_{max}	Max Grid points	Reshock	Perturbation
RUN1 (2D)	0.00625	YES	9280	576	-	1,345,280	YES	NO
RUN2 (2D)	0.00625	YES	11200	576	-	1,345,280	NO	NO
RUN3 (3D)	0.025	YES	2320	144	144	3,082,264	YES	NO
RUN4 (3D)	0.0125	YES	4640	288	288	15,350,792	YES	NO
RUN5 (3D)	0.0125	YES	5600	288	288	17,486,400	NO	NO
RUN6 (3D)	0.00625	YES	9280	576	576	45,123,912	YES	NO
RUN7 (3D)	0.0125	YES	4640	288	288	15,350,792	YES	YES
RUN8 (3D)	0.0125	YES	5600	288	288	17,486,400	NO	YES

Characteristic turbulence measures based on the simulation data are presented in Figs. 22 and 23, in terms of K spectra and integrated TKE, respectively. The K spectra is obtained as in Fig. 5 above, based on a slice of data defined around the center of the gas-curtain at z=2 cm for the nozzle. Multiple 1D *TKE* spectra were calculated along y axis, at different x locations in the mixing layer and these spectra were averaged .The turbulent kinetic energy is first bumped up as the gas-curtain is shocked(t=0); K then decreases, and then increases again at reshock – as energy is again deposited through baroclinic production of vorticity at the material interfaces; shorter wavelengths get populated as time evolves, and self-similarity of the spectra is suggested.

The effect of slight perturbation of the SF6 gas-curtain ICs was next examined. Two cases were compared: .a) all cylinders are perfectly aligned along y – was the reference (no perturbation, Fig. 24a); b) a small perturbated arrangement having std deviation of 0.1R, where R is the nozzle radius, is added to offset the location of some of the cylinders (Fig. 24b). The perturbations can be mathematically expressed as

$$\Delta x = A\sum_n a_n \sin(k_n y)$$

$$A\, is\, the\, s.d. = 0.1 \times Nozzle\, Radius$$

$$k_n = 2\pi n / L_y;\ random\, numbers: -\frac{1}{2} < a_n < \frac{1}{2}$$

where Ly is the domain length in the y direction (along the nozzles). Figures 25-28 show significant effects of the perturbed gas-curtain ICs, and compares the simulated results with those available from the laboratory experiments. The simulations predict that the perturbation of the nozzle arrangement promotes uneven growth and merging of characteristic vortical structures and enhanced mixing.

CONCLUSIONS

We report progress in testing and validating an ILES strategy to model representative shock-driven material mixing studies relying on physics capturing numerics (no explicit SGS models). The particular ILES considered is based on a nominally-inviscid simulation model that uses the LANL RAGE code. Prototypical case studies were considered for which laboratory data and/or previous LES data are available as reference. We find good agreement between ILES predictions, experiments, and previously reported simulations. The work suggests that robust effective performances can be achieved with ILES in this context.

Acknowledgements

Los Alamos National Laboratory is operated by the Los Alamos National Security, LLC for the U.S. Department of Energy NNSA under Contract No. DE-AC52-06NA25396. This work was made possible by funding from the Laboratory Directed Research and Development Program on "Turbulence by Design" at Los Alamos National Laboratory through directed research project number 20090058DR.

References

1. Sagaut P. 2006, *Large Eddy Simulation for Incompressible Flows*, 3rd Ed., Springer, NY.
2. Ghosal, S., 1996, *J. Comput. Phys.* **125**, pp. 187-206.

3. F.F. Grinstein, L.G. Margolin, and W.J. Rider 2007, Eds., *Implicit Large Eddy Simulation: Computing Turbulent Flow Dynamics*, Cambridge University Press, New York.
4. Vetter, M. & Surtevant 1995, B., *Shock Waves*, **4**, pp. 247-252.
5. Hill, D.J., Pantano, C. & Pullin, D.I. 2006, *J. Fluid Mech.*, **557**, pp. 29–61.
6. M. Gittings, *et al.* 2006, "The RAGE Radiation-Hydrodynamic Code", *Los Alamos Technical Report* LAUR-06-0027.
7. Balakumar B.J., Orlicz G., Tomkins C. and Prestridge K. 2008, *Phys. Fluids,* **20**, 124103.
8. R.L. Holmes, *et al.* 1999, *J. Fluid Mech.*, **389**, pp. 55-79.
9. C.A. Zoldi-Sood, *et al.*, "Simulations of a Reshocked Varicose Gas Curtain", *61st Annual Meeting of the APS DFD, November 23-25, 2008, San Antonio, TX.*
10. George, WK 2006, "Recent Advancements Toward the Understanding of Turbulent Boundary Layers," *AIAA Journal*, Vol..44, no.11, pp. 2435-2449.
11. Cohen, R.H. *et al.* 2002, *Physics of Fluids*, **14,** pp. 692-709.
12. M. Latini, O. Schilling, and W.S. Don 2006, in *The Physics of Compressible Turbulent Mixing, Proc. of the 10th IWPCTM*, Paris, France, pp. 349-352, M. Legrand & M. Vandenboomgaerde, eds., Paris, France.
13. D. L. Youngs, Rayleigh–Taylor and Richtmyer–Meshkov Mixing, Chapter 13 in *Implicit Large Eddy Simulation: Computing Turbulent Fluid Dynamics*, F.F. Grinstein, L.G. Margolin, and W.J. Rider, eds., Cambridge University Press, 2007.
14. Jiménez, J., Wray, A., Saffman, P. , and Rogallo, R. 1993, *J. Fluid Mech.*, **255**, pp. 65-90.
15. D. Drikakis, C. Fureby, F.F. Grinstein, and D. Youngs, *J. of Turbulence*, **8**, 020, 2007.
16. V.G. Weirs, T. Dupont, and T. Plewa 2008, *Physics of Fluids*, **20**, 044102.
17. Gowardhan A.A. 2008, *Ph.D. dissertation*. University of Utah.

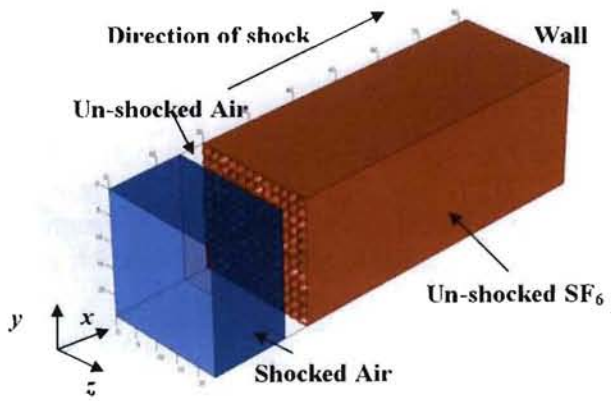

Figure 1. Schematic of the planar shocktube domain.

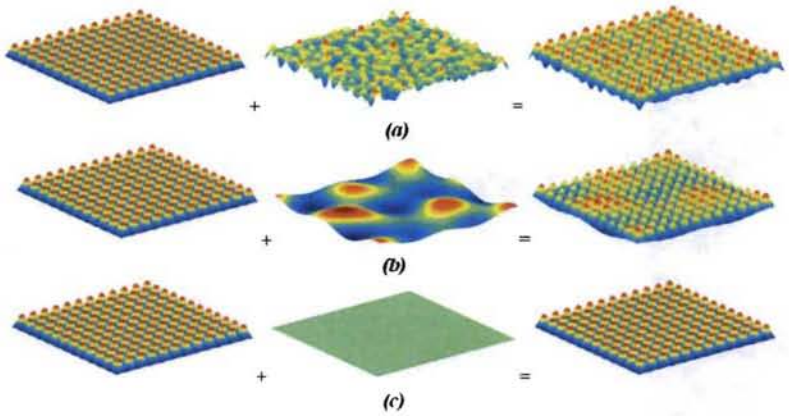

Figure 2. Visualization of the initial interface conditions tested in terms of distributions of the SF_6 mass-fraction; (a) short wave perturbed IC (b) long wave perturbed IC (b) no IC perturbation.

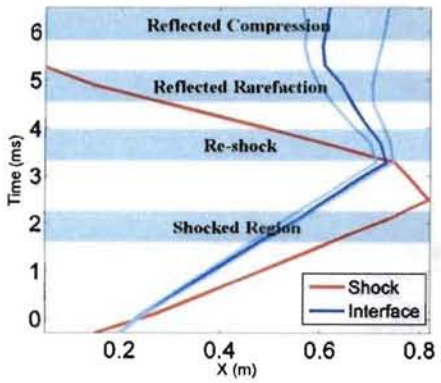

Figure 3: Shock-interface diagram for a representative planar shock-tube simulation.

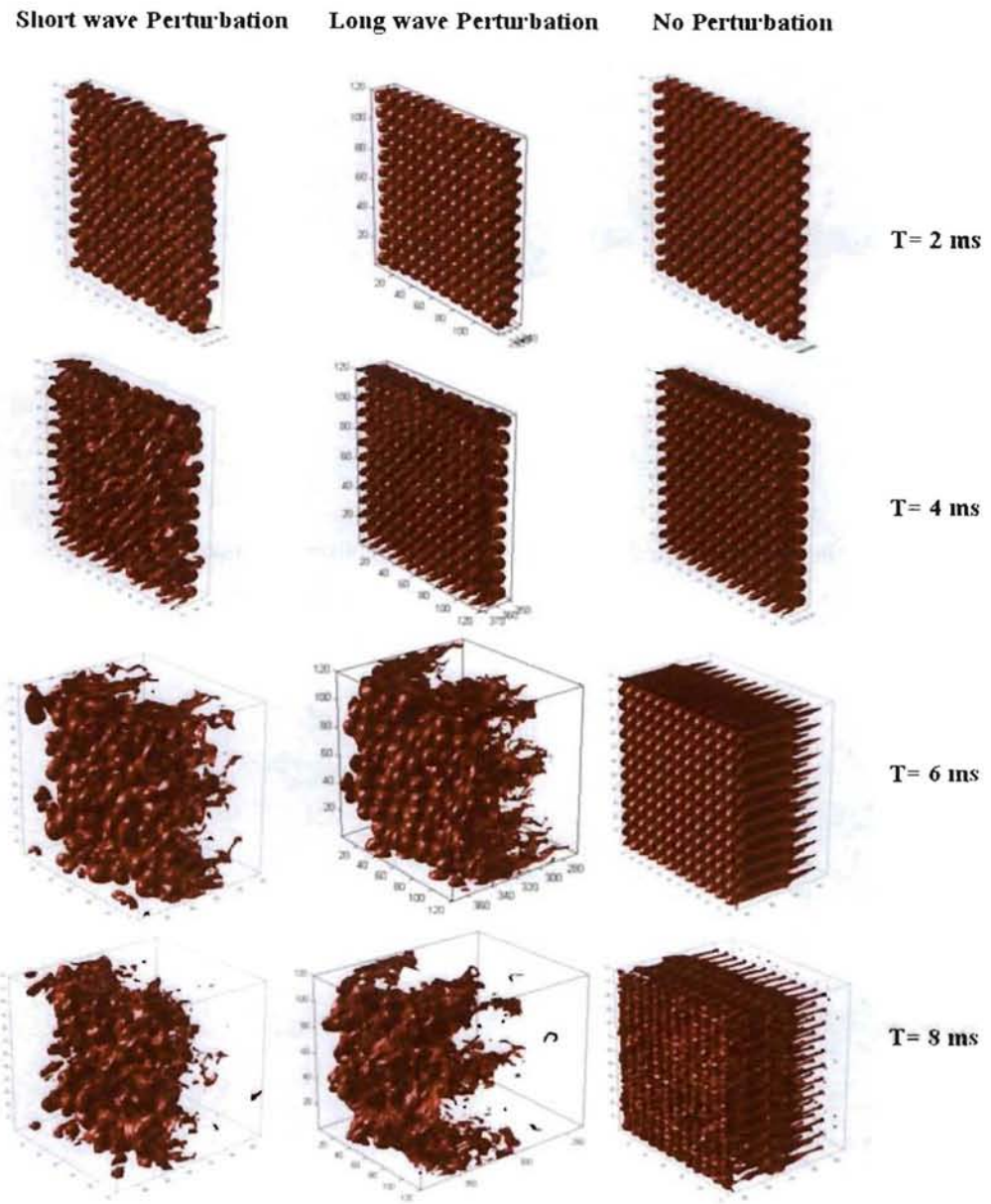

Figure 4. Isosurfaces of SF_6 mass-fraction at t = 2 ms, 4 ms, 6ms, 8 ms for the *short*, *long* and *no* perturbation cases.

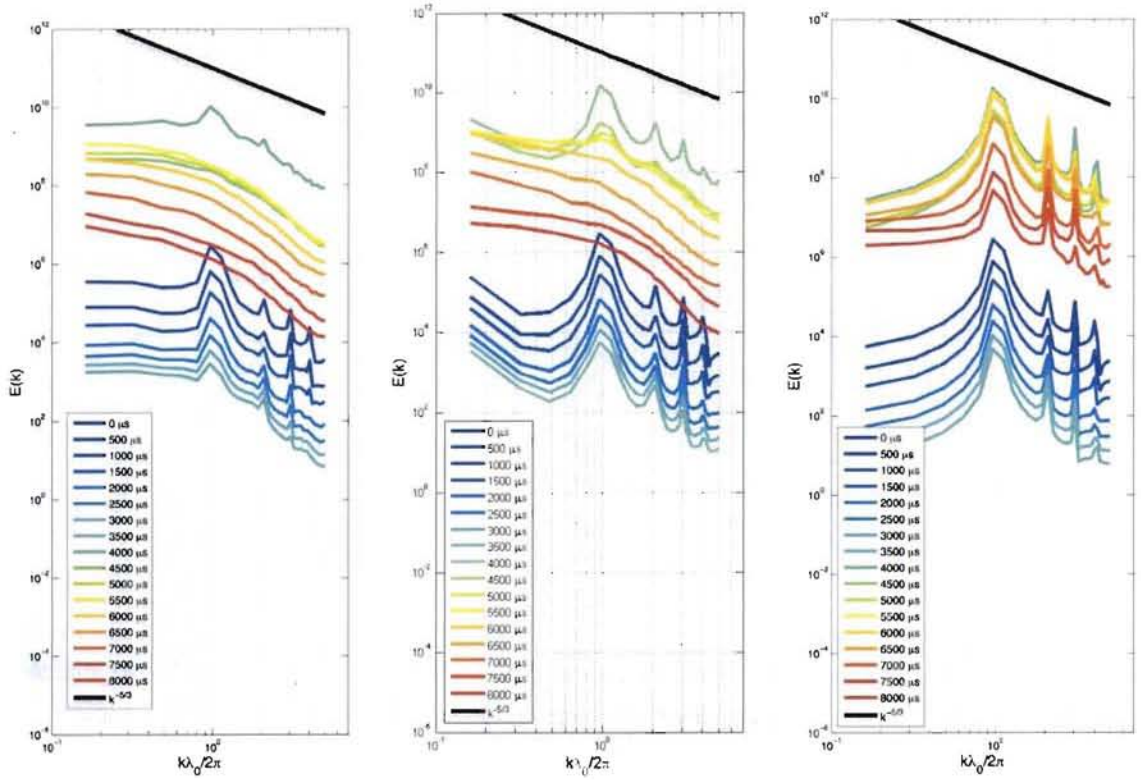

(a) *(b)* *(c)*

Figures 5. Spectra of the Turbulent Kinetic Energy *K* for the *short (a)*, *long* (b) and *no* perturbation (c) cases.

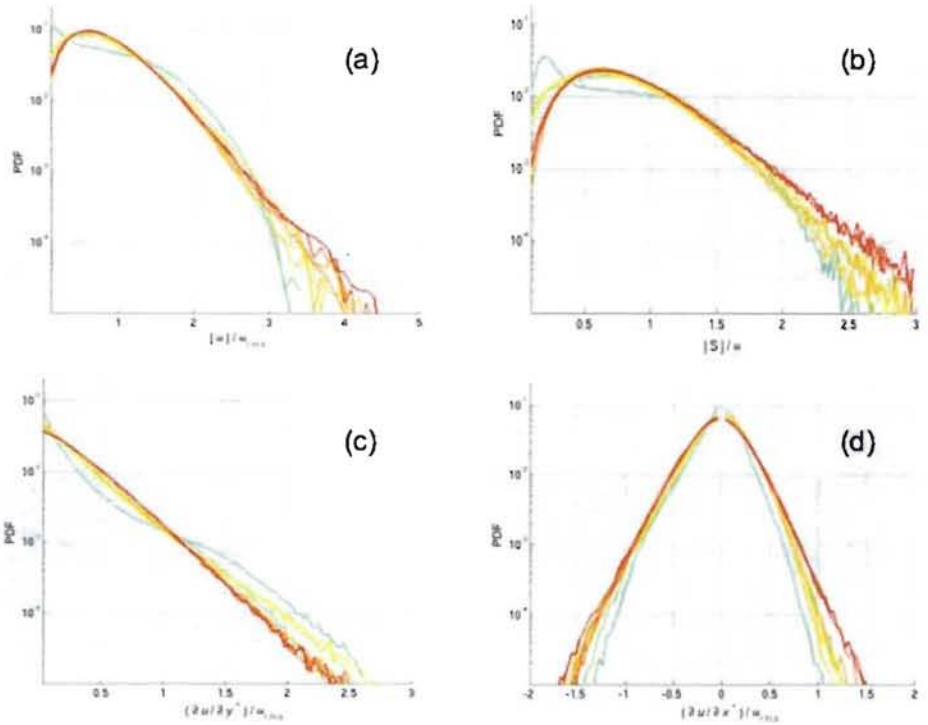

Figure 6. PDFs of characteristic velocity functions for the short perturbation case; a) vorticity magnitude, b) strain-rate magnitude, c) transverse velocity derivatives, d) longitudinal velocity derivatives; colors correspond to the same times as in Fig. 5; the time-dependent root-mean-square of the vorticity magnitude, w_{rms} is used as scale in all cases.

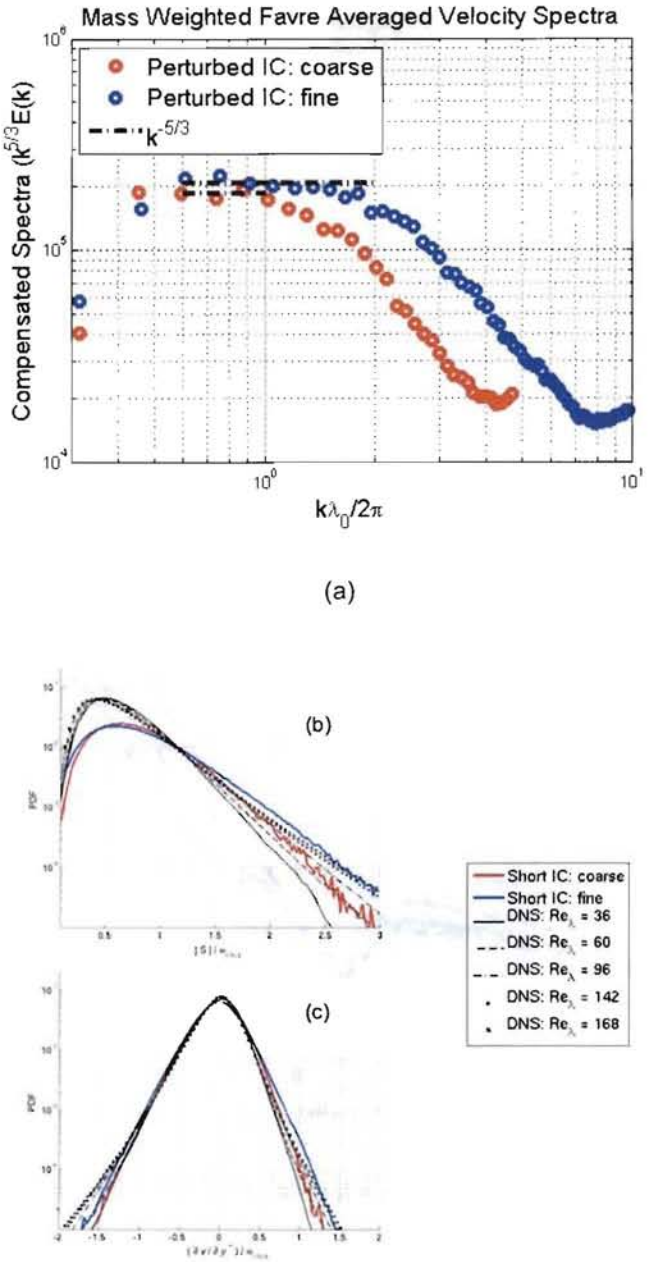

Figure 7. Effects of grid resolution on late-time results for the *randomly perturbed* case (RUN4 & RUN6, t=8.0 ms), and comparisons with DNS data of incompressible isotropic turbulence [12]; a) compensated *TKE* spectra, b) PDF of strain-rate magnitude, c) PDF of longitudinal velocity derivatives.

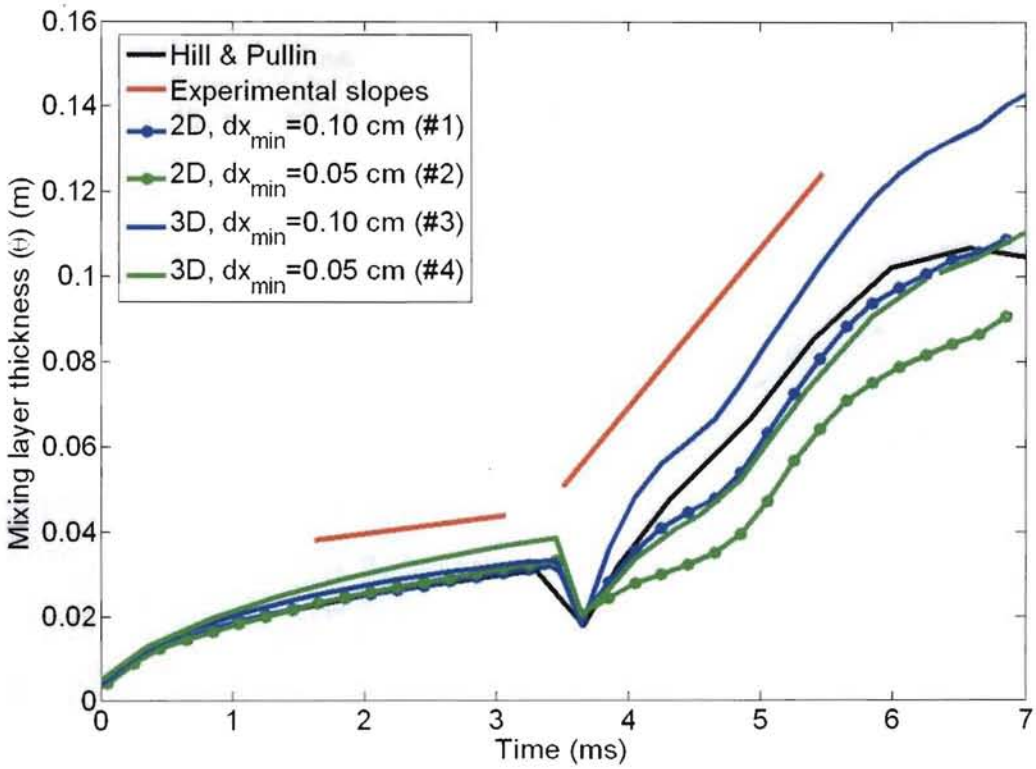

Figures 8a. Variation of mixing layer thickness as a function of time for the *randomly perturbed* case (RUN1- RUN4).

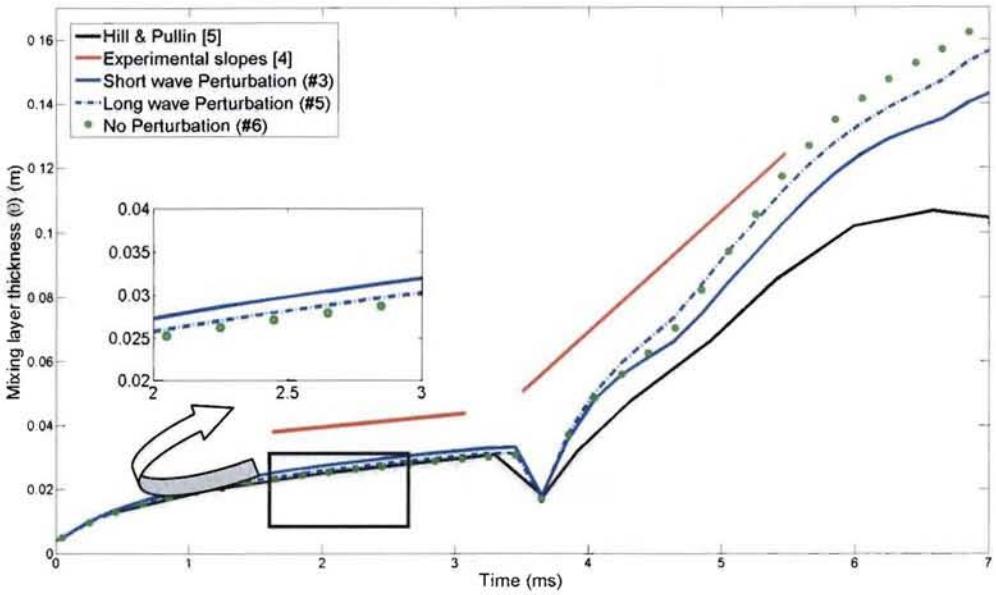

Figures 8b. Variation of mixing layer thickness as a function of time, for the *randomly perturbed* and non-perturbed IC cases (RUN3, RUN5).

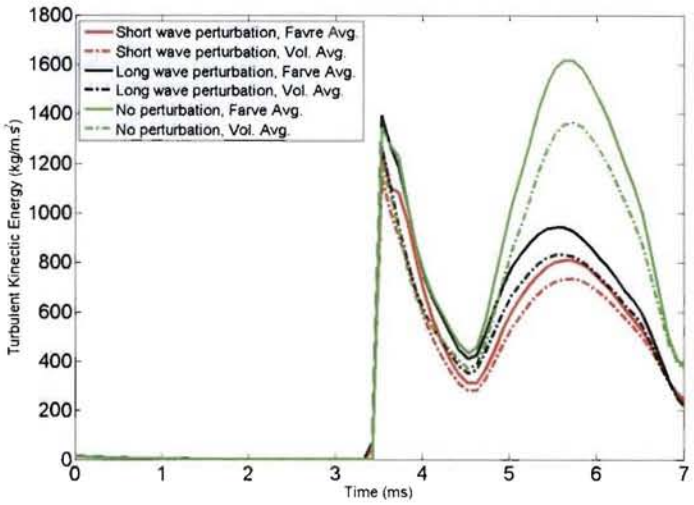

Figure 9. IC effects on time-series of integrated turbulent kinetic energy.

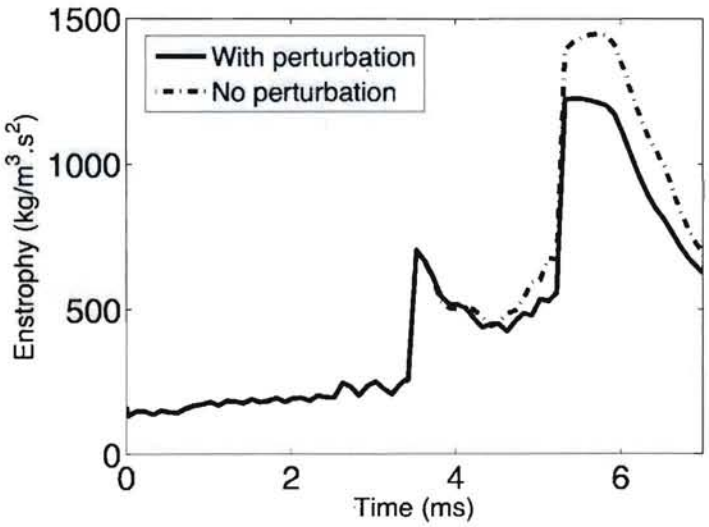

Figure 10. IC effects on time-series of mass-weighted enstrophy.

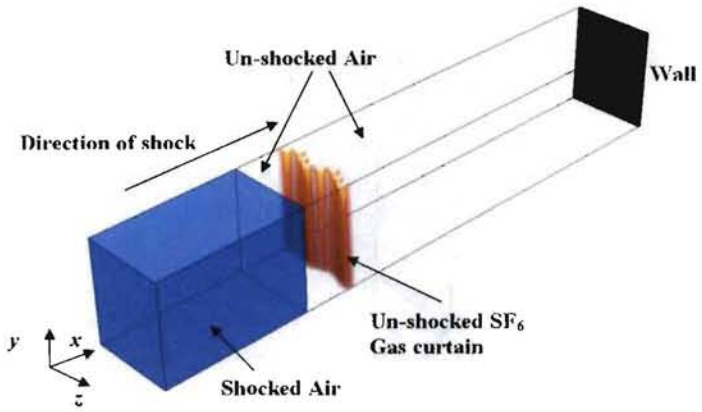

Figure 11: Schematic of the Gas-Curtain Shock-Tube.

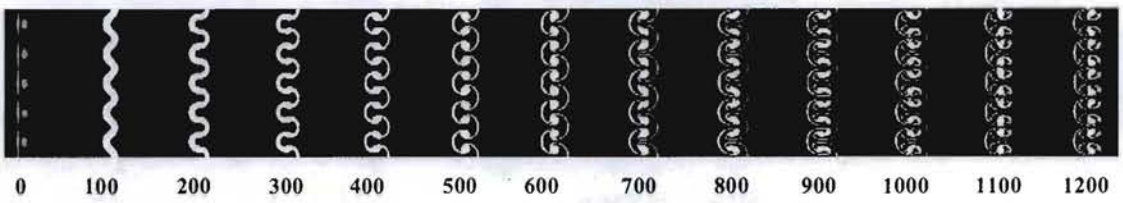

Figure 12: Detailed 2D RMI simulation in gas-curtain shocktube experiments without reshock for the M=1.20 case (left to right: 0-1200 μs), in terms of SF6 concentration distributions.

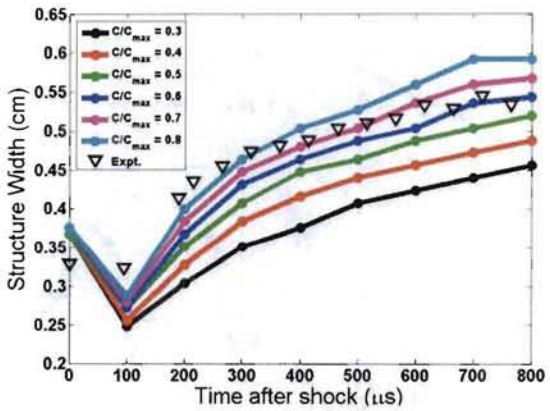

Figure 13: Structure width as a function of C_{max}.

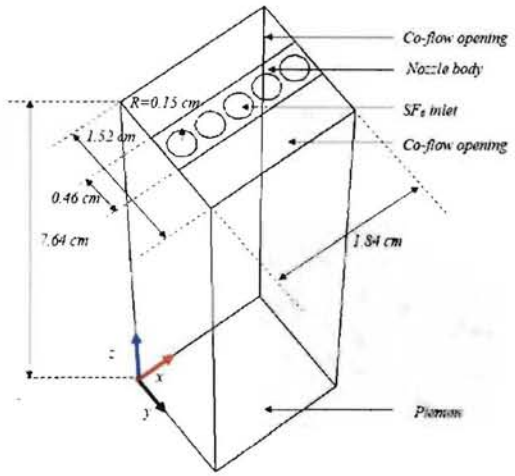

Figure 14: Schematic of the computation domain in the IC simulation.

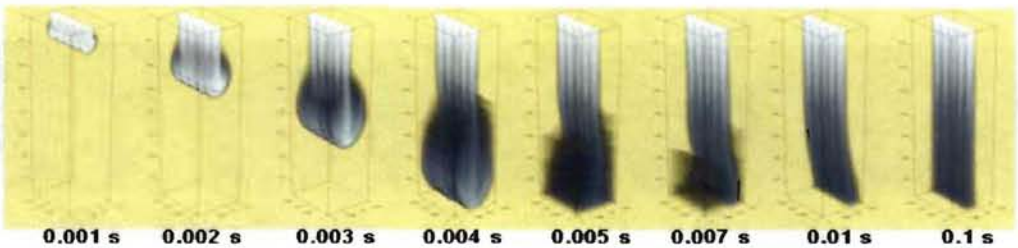

Figure 15: Evolution of the IC simulation in time.

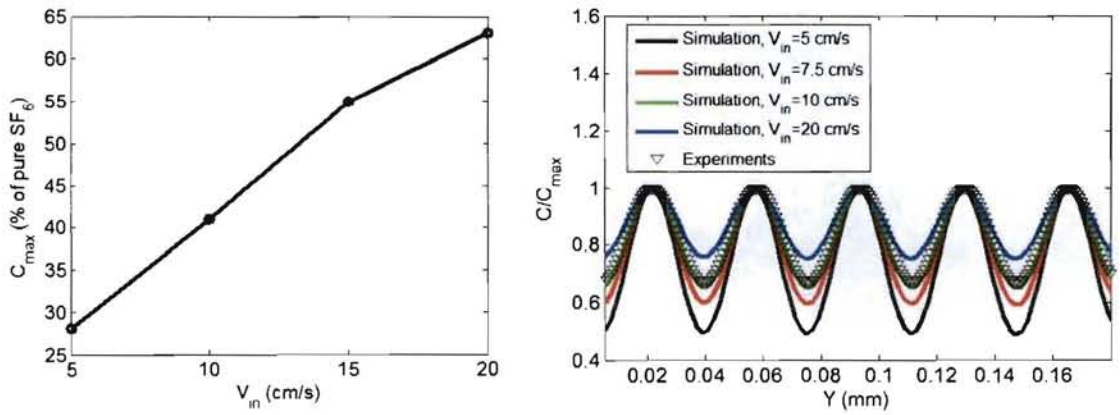

Figure 16: Variation of (a) Cmax and (b) C/Cmax pfrofile along y axis as a function fo jet exit velocity.

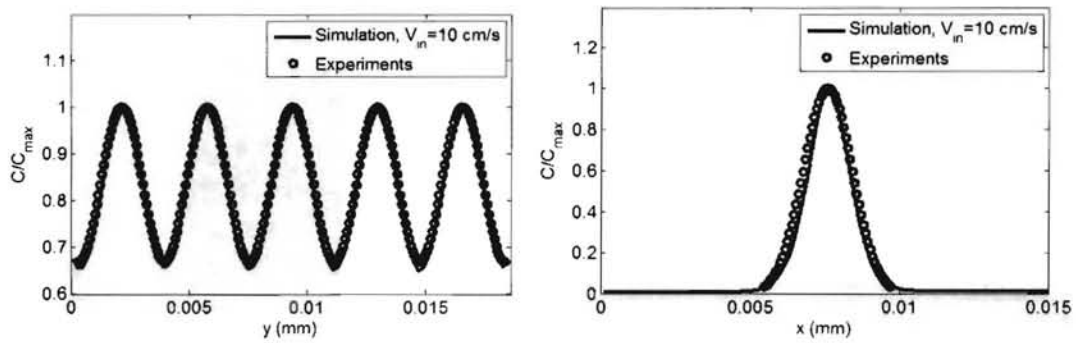

Figure 17: Best matched simulation: Variation of normalized concentration (C/Cmax) along (a) y axis and (b) x axis passing thorugh the center of gas curtain.

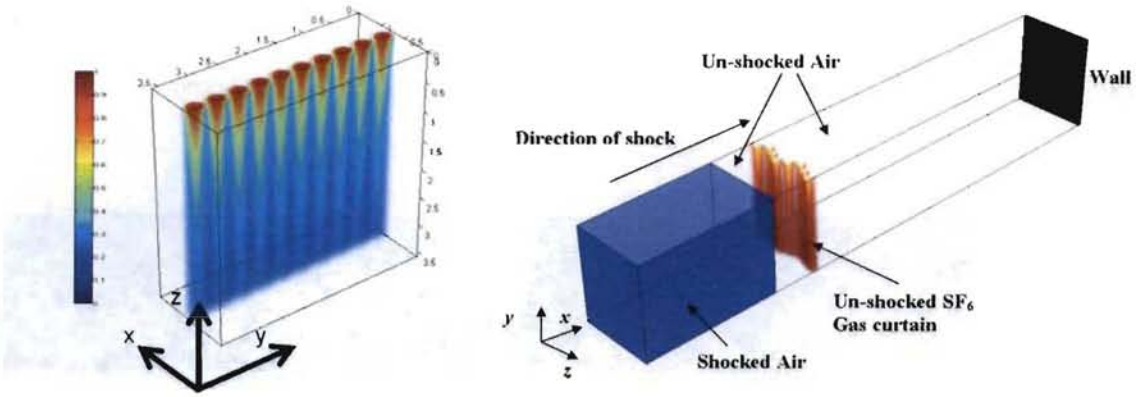

(a) (b)

Figure 18: (a) RAGE input (distribution of SF6 volume fraction) (b) Schematic of the RAGE computational domain.

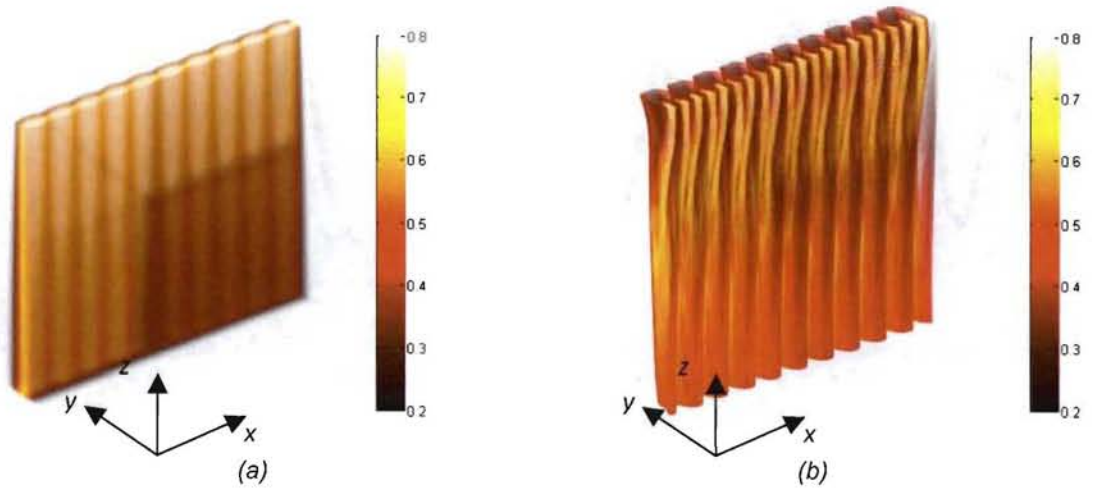

Figure 19: Shocked Gas-Curtain; 3D visualization of SF_6 mass fraction at (a) *t=0;* (b) *t=600.*

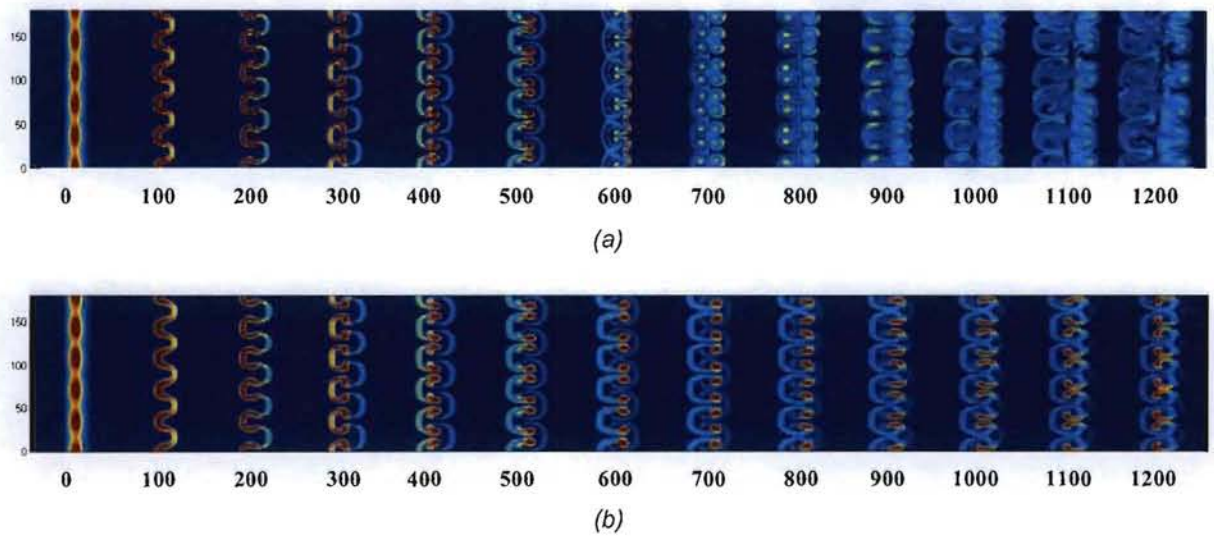

Figure 20: Visualization of SF6 mass fraction as a time series a) reshocked, b) no reshock

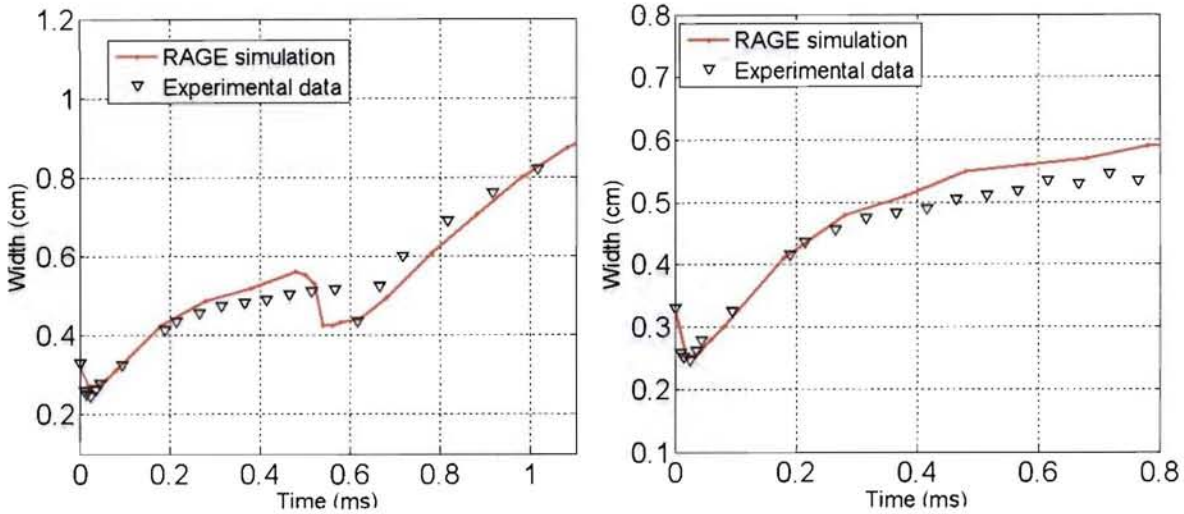

Figure 21: Mixedness growth curve for a) reshocked, b) no reshock

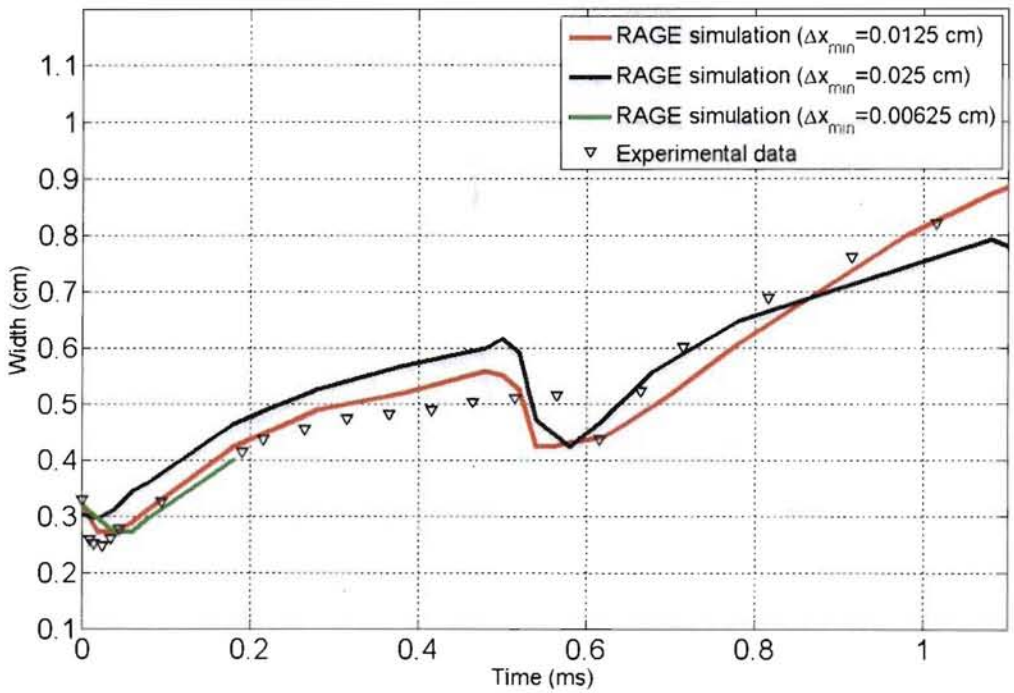

Figure 22: Effects of grid resolution on mixedness growth: reshocked case

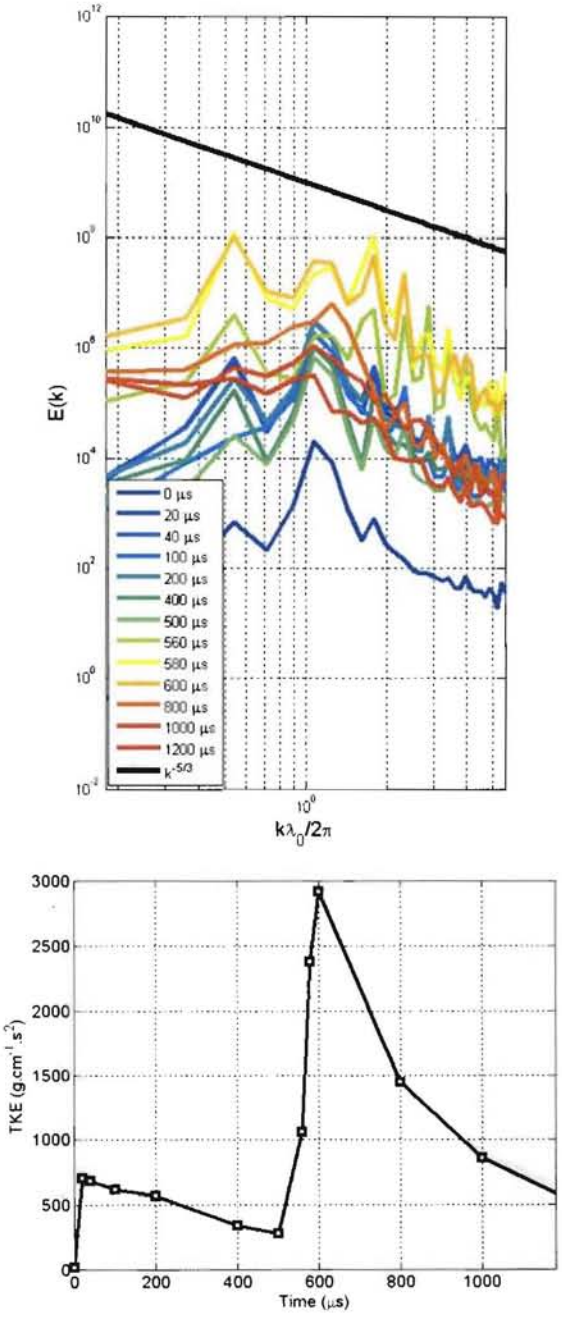

(a) *(b)*

Figure 23: (a) *K* spectra (b) TKE time series

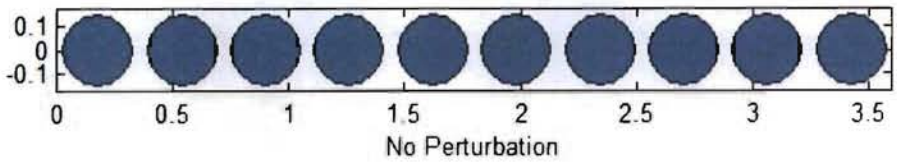

(a)

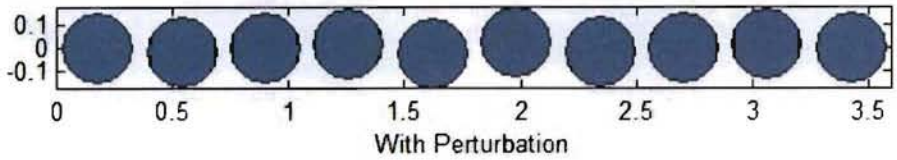

(b)

Figure 24: Shematic of the nozzle arrangements for: a) no perturbation and b) with perturbation.

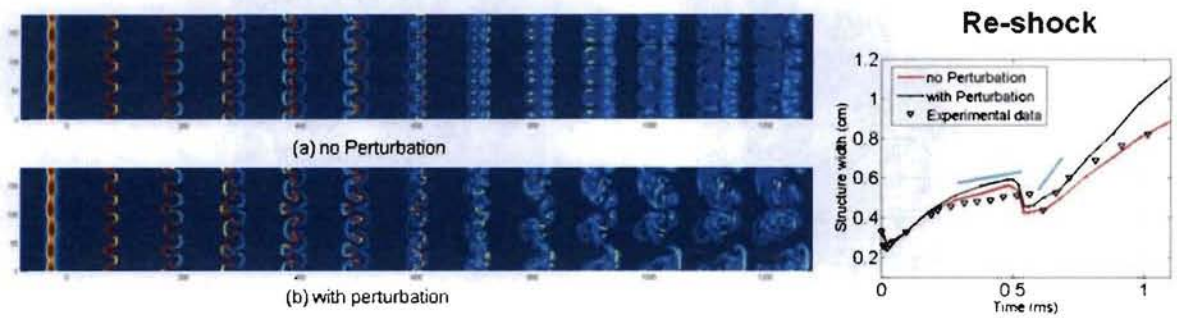

Figure 25: Visualizations of the reshocked gas-curtain: a) no perturb. b) with perturb.

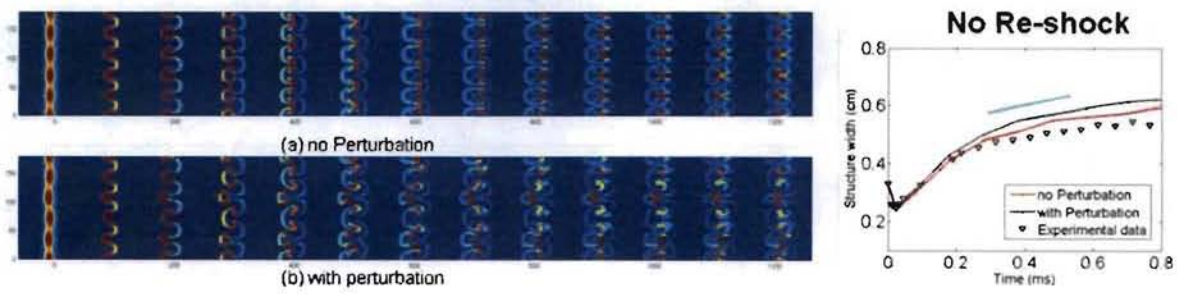

Figure 26: Visualizations of the non-reshocked gas-curtain: a) no perturb. b) with perturb.

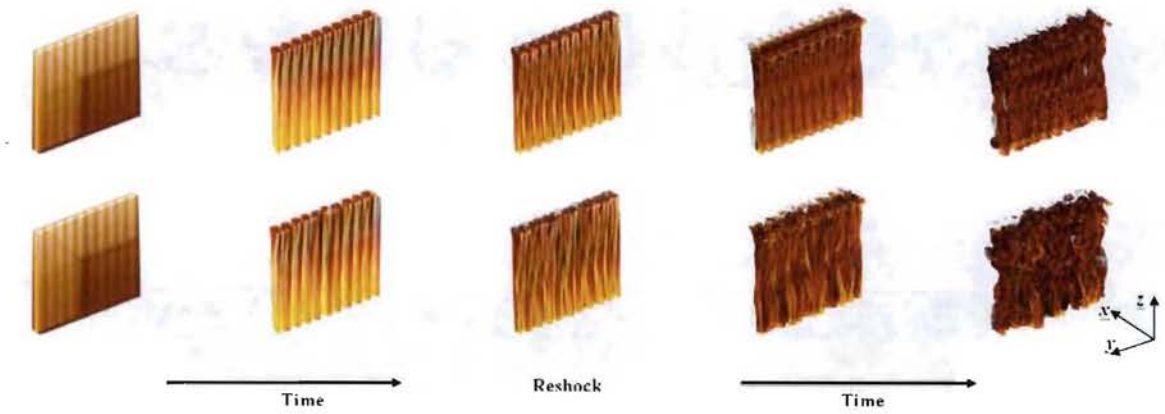

Figure 27: 3D visualization of SF6 mass fraction: no perturb (top), with perturb. (bottom)

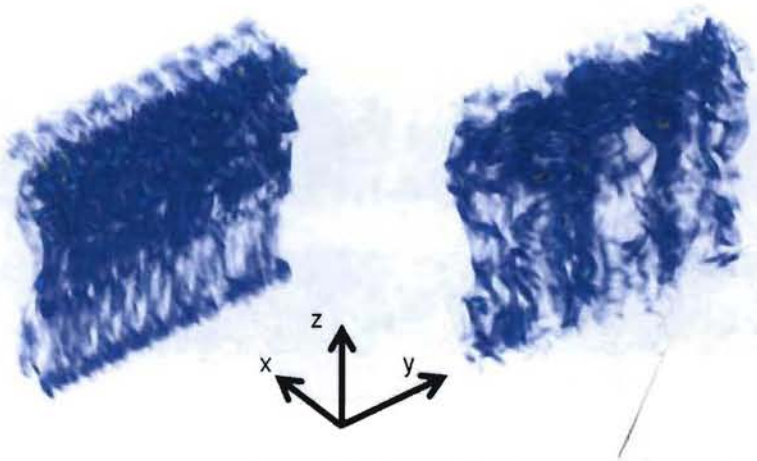

Figure 28: 3D visualization of vorticity magnitude at late time (t=1200 micro-sec) after reshock, left: no perturb. right: with perturb.